

QUAMO: QUATERNION MOTIONS FOR VISION-BASED 3D HUMAN KINEMATICS CAPTURE

Cuong Le¹, Pavlo Melnyk¹, Urs Waldmann¹, Mårten Wadenbäck¹, Bastian Wandt²

¹ Linköping University, Sweden

² Independent researcher

cuong.le@liu.se

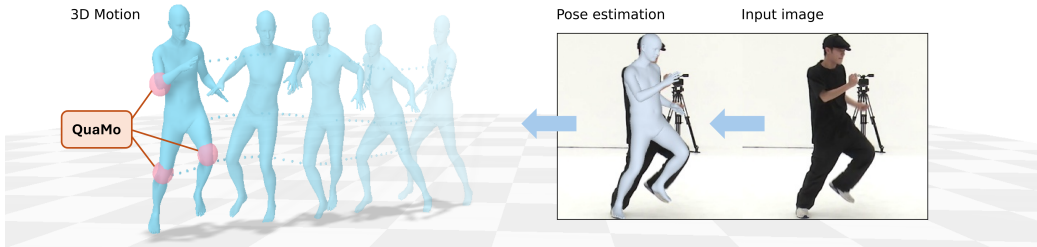


Figure 1: We present **QuaMo**, a novel online 3D human kinematics capture approach based on **Quaternion Motions** (pink), modeled via a meta-PD algorithm with acceleration enhancement. Given a vision-based 3D pose estimation as prior, QuaMo predicts plausible and accurate motions.

ABSTRACT

Vision-based 3D human motion capture from videos remains a challenge in computer vision. Traditional 3D pose estimation approaches often ignore the temporal consistency between frames, causing implausible and jittery motion. The emerging field of kinematics-based 3D motion capture addresses these issues by estimating the temporal transitioning between poses instead. A major drawback in current kinematics approaches is their reliance on Euler angles. Despite their simplicity, Euler angles suffer from discontinuity that leads to unstable motion reconstructions, especially in online settings where trajectory refinement is unavailable. Contrarily, quaternions have no discontinuity and can produce continuous transitions between poses. In this paper, we propose QuaMo, a novel Quaternion Motions method using quaternion differential equations (QDE) for human kinematics capture. We utilize the state-space model, an effective system for describing real-time kinematics estimations, with quaternion state and the QDE describing quaternion velocity. The corresponding angular acceleration is computed from a meta-PD controller with a novel acceleration enhancement that adaptively regulates the control signals as the human quickly changes to a new pose. Unlike previous work, our QDE is solved under the quaternion unit-sphere constraint that results in more accurate estimations. Experimental results show that our novel formulation of the QDE with acceleration enhancement accurately estimates 3D human kinematics with no discontinuity and minimal implausibilities. QuaMo outperforms comparable state-of-the-art methods on multiple datasets, namely Human3.6M, Fit3D, SportsPose and AIST. The code is available at [Q](https://github.com/cuongle/QuaMo).

1 INTRODUCTION

Monocular 3D human motion capture is a challenging problem in computer vision due to the loss of depth information and the complexity of body articulation. Traditional 3D human pose estimation (HPE) approaches, which directly estimate 3D joint positions or angles, achieve high accuracy on distance-based evaluation metrics (Pavllo et al., 2019; Zheng et al., 2021; Kocabas et al., 2020; Sun et al., 2023; Goel et al., 2023). However, when considering a captured trajectory over consecutive

frames from a video, 3D HPE often results in implausible artifacts such as jittery or unnatural poses. Addressing these challenges by introducing physics models (*i.e.*, state-space model with velocity and acceleration) to enforce temporal consistency between consecutive poses is an emerging research direction, fusing vision-based predictions with human kinematic chains (Shimada et al., 2020) or volumetric models (Loper et al., 2015). Our proposed method, QuaMo, falls into this category.

The foundation of all kinematics-based approaches is the nonlinear state-space model, where human poses and their corresponding velocities are computed from either meta-PD controllers with learnable PD gains (Shimada et al., 2021; Li et al., 2022a; Le et al., 2024a), physics simulation engines (Yuan et al., 2021; Gartner et al., 2022b;a), or neural networks (Rempe et al., 2021). Using state-space modeling, the process of predicting the next human poses is equivalent to solving a time-series ordinary differential equation (ODE) (Chen et al., 2018). Our proposed method, QuaMo, serves as the function that takes the current human pose as input and predicts the corresponding velocity, giving an estimate for the next pose. We develop QuaMo as an online approach, only relying on the single time step input, making QuaMo applicable to real-time applications (autonomous driving (Priisalu et al., 2020; Wang et al., 2024), or biomechanics (Bogert et al., 2013; Uhlrich et al., 2023)).

Current modern temporal-based approaches often opt for Euler angles (Yuan et al., 2021; Rempe et al., 2021; Li et al., 2022a) as the main joint orientation representation for human kinematics estimation. Despite their simplicity and intuitive interpretation, Euler angles have two well-known issues: singularities (a.k.a. gimbal lock) and discontinuities (at angles 0 and 2π) (Shoemake, 1985). Discontinuities cause the joint to incorrectly rotate backwards to the intended direction, resulting in highly unstable motion reconstructions. Quaternions are known to resolve the discontinuity problem by representing orientations with a four-dimensional vector, but have not received proper studies within the field. To this end, we propose using quaternion joints for kinematics estimation, with their velocity computed from a novel acceleration enhanced PD control. Unlike Euler angles, the quaternion derivative cannot be approximated by a finite difference between respective elements due to rotational constraints (Kuipers, 1999) – we use an operation based on the Hamilton product.

The underlying state-space model of QuaMo consists of a joint orientation represented as a quaternion and an angular velocity state, resulting in two main parallel streams (Fig. 2): 1) a quaternion first-order derivative calculation based on the Hamilton product between the current quaternion and the newly computed angular velocity, and 2) a meta-PD algorithm with newly developed acceleration enhancement to estimate the rotational velocity derivative. Unlike prior work (Shimada et al., 2021; Le et al., 2024a), we apply the exact quaternion integration solution under unit sphere constraint, eliminating any approximation errors that arise when using the traditional Euler integration (a.k.a. first-order Runge–Kutta) method (Andrle & Crassidis, 2013). The novel acceleration enhancement term, computed based on the second-order quaternion difference between reference poses, adaptively compensates the signals of the PD algorithm for more accurate kinematics estimates. Specifically, the acceleration term increases the control signals when sudden pose changes occur (fast movement) and dampens the signals upon reaching the target poses. A demonstration of our proposed approach can be seen in Fig. 1.

Our proposed approach is evaluated against current state-of-the-art kinematics-based methods on the Human3.6M (Ionescu et al., 2014), Fit3D (Fieraru et al., 2021), SportsPose (Ingwersen et al., 2023), and a subset of AIST (Li et al., 2021b) datasets. In summary, our main contributions are:

- We propose a quaternion differential equation with quaternion as joint rotation for 3D human motion estimation, inherently overcoming the drawbacks of Euler angles.
- We introduce a novel acceleration enhancement that adaptively regulates the angular acceleration based on quick movement changes for more accurate motion estimation.
- We show that solving the QDE under the quaternion unit-sphere constraint \mathcal{S}^3 results in more plausible and accurate human poses in online real-time settings.

2 RELATED WORK

3D Human Pose Estimation. Traditionally, 3D human motion capture is addressed via 3D pose estimations, either 1) lifting from 2D cues (Wang et al., 2019; Pavllo et al., 2019; Wandt & Rosenhahn, 2019; Li et al., 2020; Xu et al., 2020; Wandt et al., 2021; Zheng et al., 2021; Zhao et al., 2023; Peng et al., 2024; Cai et al., 2024; Sun et al., 2024; Lang & Chuah, 2025; Huang et al., 2025; Kim et al., 2025), or 2) directly estimating 3D human poses from input images (Pavlakos et al., 2017;

Kocabas et al., 2020; Li et al., 2021a; 2022b; You et al., 2023; Wang & Daniilidis, 2023; Kim et al., 2023; Baradel et al., 2024; Dwivedi et al., 2024; Le et al., 2024b; Patel & Black, 2025). Despite the low average joint error, methods lifting from 2D do not consider the human body constraint, *i.e.* bone-length consistency between consecutive 3D poses, thus cannot be compared to template-based approaches, and this argument has been raised by related work (Gärtner et al., 2022a; Li et al., 2022a; Zhang et al., 2024). To impose natural body constraints, modern approaches utilize volumetric human models such as SMPL (Loper et al., 2015) as a prior and only estimate the angular poses for the models, fitting them to 2D and 3D observations (Pavlakos et al., 2019; Kanazawa et al., 2019; Mahmood et al., 2019; Zhu et al., 2023). This line of research often overlooks the temporal consistency between consecutive estimated poses, leading to implausible artifacts such as jittery, foot-skating, and unnatural poses. In this work, we address these issues by employing a kinematics-based approach, taking into account the temporal consistency between consecutive 3D estimations.

3D Human Kinematics Capture. Unlike 3D HPE, human kinematics approaches enforce temporal consistency to eliminate motion artifacts created by monocular estimation, either through pose priors (Huang et al., 2022; Rempe et al., 2021), or physics laws and constraints (Shimada et al., 2020; Gärtner et al., 2022a; Li et al., 2022a; Tripathi et al., 2023; Zhang et al., 2024).

Trajectory optimization is a popular approach for kinematics-based 3D human motion capture (Al Borno et al., 2013; Shimada et al., 2020; Rempe et al., 2020; Xie et al., 2021; Gärtner et al., 2022b;a). These approaches commonly introduce kinematics constraints in the form of physics laws as their main optimization objective. This poses a challenge where the physical constraints are required to be differentiable and the optimization is often done offline. Recent approaches extend the physics modeling with comprehensive contact estimations from modern physics engines Coumans & Bai (2016–2019); Todorov et al. (2012). However, these contact models are non-differentiable, motivating a subfield of motion imitation research that utilizes reinforcement learning with physics constraints in their reward designs (Yu et al., 2021; Yuan et al., 2021; Peng et al., 2022; Yao et al., 2022; Huang et al., 2022; Yuan et al., 2023). A major problem with trajectory optimization and reinforcement learning is the limited adaptation to unseen motions.

Recently, learning 3D human kinematics from data has received more attention, thanks to its strong generalization capability. Rempe et al. (2021) use a conditional variational autoencoder to generate the next human pose, implicitly treating the latent variables as motion kinematics. While the latent kinematics is learned, Rempe et al. (2021) still require a test time optimization process to refine their estimation. In contrast, leveraging off-the-shelf monocular 3D HPE (Kocabas et al., 2020; Li et al., 2022b) as the targets for motion reconstruction can alleviate the offline optimization while retaining robust and physically plausible kinematics estimation. Zhang et al. (2024) utilize a transformer-based autoencoder that takes the full sequence of monocular 3D poses as inputs, predicts the corresponding sequence while enforcing physics constraints in the latent space. To maintain the explicit temporal consistency between frame-wise predictions, Shimada et al. (2021) introduces the usage of a meta-PD controller for predicting the motion dynamics based on the 2D pose cues estimated from video. While the 3D kinematics capture works online, Shimada et al. (2021) still require a pre-filtering of 2D cues to ensure plausible 3D estimations. Li et al. (2022a) apply the PD controller with temporal convolutions and an attentively refined target pose from the full sequence for robust motion estimation. The key similarity between these approaches is the access to future monocular cues, preventing them from real-time deployments. Le et al. (2024a) address the imperfection of *online* PD-based simulation by re-integrating the input poses into the final prediction via a learnable Kalman filter. However, re-introducing noisy kinematics has the potential to break the temporal consistency enforced by the integration scheme. Furthermore, one source of error for poor simulations is the usage of Euler angles that are prone to representation changes when enforcing temporal consistency frame-wise (Allgeuer & Behnke, 2018; Yang, 2019).

Our work contributes towards the online 3D human kinematics capture, using a meta-PD algorithm with the robust quaternions as the joint orientation representation. The kinematics estimation follow the correct Lie-group constrained calculation for quaternions, while additionally damped by a novel second-order control compensation that results in smoother and more accurate motions.

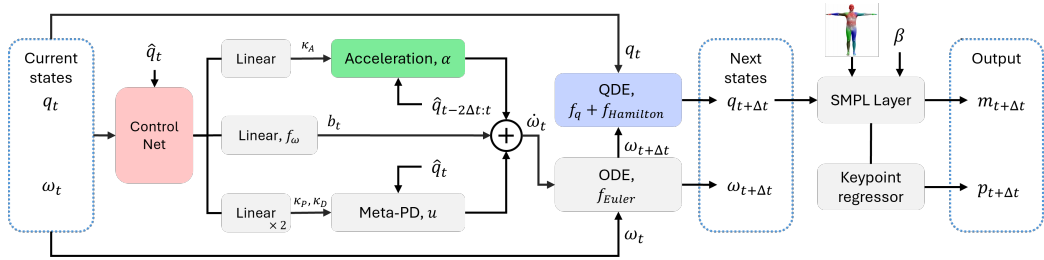


Figure 2: QuaMo consists of two differentiable equations: ODE for angular velocity ω and QDE for quaternion pose q . The updated $\omega_{t+\Delta t}$ is computed via a data-driven meta-PD controller with the additional adaptive signals from our novel second-order acceleration enhancement and Euler integration. Given $\omega_{t+\Delta t}$, the next human pose $q_{t+\Delta t}$ is updated by solving the QDE with the Hamilton quaternion product. The human body mesh $m_{t+\Delta t}$ and the corresponding keypoints $p_{t+\Delta t}$ are retrieved by applying a linear transformation with the SMPL skinned model from Pavlakos et al. (2019), taking the pose $q_{t+\Delta t}$ and shape parameter β as inputs.

3 METHODOLOGY

3.1 OVERALL PIPELINE

We model human motion via a state-space system. Given N joints in the human body, let $Q \in \mathbb{R}^{N \times 4}$ be the human pose tensor consisting of joint relative rotations represented as N quaternions $q \in \mathbb{H}$ (the Hamilton set). The corresponding angular velocities are denoted as $\omega \in \mathbb{R}^3$. We use the SMPL body model from Loper et al. (2015) with $N = 24$ body joints with the root rotation at the first entry. The discrete-time state-space model of the system with a sampling rate of Δt is

$$\begin{bmatrix} \omega_{t+\Delta t} \\ q_{t+\Delta t} \end{bmatrix} = \begin{bmatrix} f_{\text{Euler}}(\omega_t, \dot{\omega}_t, \Delta t) \\ f_{\text{Hamilton}}(q_t, \dot{q}_t, \Delta t) \end{bmatrix}, \quad \begin{bmatrix} \dot{\omega}_t \\ \dot{q}_t \end{bmatrix} = \begin{bmatrix} f_{\omega}(q_t, \omega_t) + u(q_t, \omega_t, \hat{q}_t) + \alpha(\hat{q}_{t-2\Delta t:t}) \\ f_q(q_t, \omega_{t+\Delta t}) \end{bmatrix}, \quad (1)$$

where \dot{q}_t and $\dot{\omega}_t$ are the first-order derivatives of q and ω at time step t , which can also be referred as the quaternion velocity and angular acceleration; $q_{t+\Delta t}$ and $\omega_{t+\Delta t}$ are the pose and angular velocity at the next time step $t + \Delta t$. The function f_{Euler} estimates the next-step angular velocity via Euler integration. The function f_{Hamilton} estimates the next-step quaternion pose using Hamilton operations. The angular acceleration $\dot{\omega}_t$ is modeled via three functions: 1) a data-driven f_{ω} that directly predicts the acceleration given the current states q_t and ω_t ; 2) an external control signal u based on the meta-PD algorithm given the reference pose \hat{q}_t from an off-the-shelf 3D pose estimator; and 3) a novel acceleration enhancement term α computed from the last three reference poses $\hat{q}_{t-2\Delta t:t}$. The quaternion velocity \dot{q}_t rotates the current pose q_t to $q_{t+\Delta t}$ along the unit sphere S^3 group of quaternion multiplication (Andrle & Crassidis, 2013). Fig. 2 shows how we build our pipeline with these functions. The predicted pose $q_{t+\Delta t}$ is used to control an SMPL model together with a shape parameter $\beta \in \mathbb{R}^{10}$, resulting in a human mesh $m_{t+\Delta t} \in \mathbb{R}^{6890 \times 3}$. We apply a joint regressor to obtain the keypoint pose $p_{t+\Delta t} \in \mathbb{R}^{17 \times 3}$, *i.e.* the 17 keypoints from Ionescu et al. (2014), or the COCO 17 keypoints from Lin et al. (2014).

3.2 QUATERNION DIFFERENTIAL EQUATION

A quaternion $q \in \mathbb{H}$ is represented by $(q_0, q_1, q_2, q_3) \in \mathbb{R}^4$, also written as:

$$q = q_0 + q_1 i + q_2 j + q_3 k, \quad (2)$$

where i , j , and k are imaginary units satisfying $i^2 = j^2 = k^2 = ijk = -1$. The sum of two quaternions p and q is obtained by summing their respective scalar coefficients: $p + q = (p_0 + q_0) + (q_1 + p_1)i + (q_2 + p_2)j + (q_3 + p_3)k$. The (Hamilton) product \otimes of two quaternions is defined as $p \otimes q = (p_0q_0 - p_1q_1 - p_2q_2 - p_3q_3) + (p_1q_0 + p_0q_1 + p_3q_2 - p_2q_3)i + (p_2q_0 + p_3q_1 + p_0q_2 + p_1q_3)j + (p_3q_0 + p_2q_1 - p_1q_2 + p_0q_3)k$, with the crucial non-commutative property $p \otimes q \neq q \otimes p$. The non-commutativity of the Hamilton product is key to *unit* quaternions, *i.e.* quaternions normalized to unit length, $\|q\| = 1$, being broadly used to represent 3D rotations, with a number of advantages over other representations, *e.g.*, gimbal lock and discontinuity avoidance. For a unit quaternion $q \in S^3$, $q_0 = \cos(\alpha/2)$ is the scalar part and $(q_1, q_2, q_3) = e \sin(\alpha/2)$ is the vector part representing a rotation about axis $e \in \mathbb{R}^3$ by angle α .

Quaternion derivative over time, \dot{q} , is an important concept in various fields including robotics, physics, and engineering (*e.g.*, in spacecraft modeling Yang (2019); Fresk & Nikolakopoulos (2013); Gołębek et al. (2022)). Given the angular velocity $\omega = (\omega_1, \omega_2, \omega_3) \in \mathbb{R}^3$, the corresponding quaternion velocity is defined via the following *quaternion differential equation* (QDE):

$$\dot{q} = \frac{1}{2}\Omega(\omega)q = \frac{1}{2} \begin{bmatrix} -[\omega]_x & \omega \\ -\omega^\top & 0 \end{bmatrix} q, \quad \text{where } [\omega]_x = \begin{bmatrix} 0 & -\omega_3 & \omega_2 \\ \omega_3 & 0 & -\omega_1 \\ -\omega_2 & \omega_1 & 0 \end{bmatrix}. \quad (3)$$

In this work, the QDE effectively describes the quaternion transitioning between 3D human poses without any representation discontinuity. Assuming constant angular velocity ω_t during Δt , the quaternion pose solution to Eq. 3 at time step $t + \Delta t$ can be written as

$$q_{t+\Delta t} = \exp\left(\frac{\Delta t}{2}\Omega(\omega_{t+\Delta t})\right)q_t = q_\omega \otimes q_t, \quad (4)$$

where $\exp(\frac{\Delta t}{2}\Omega(\omega))$ is the rotation matrix, that rotates q_t using ω_t . Equivalently, the next pose $q_{t+\Delta t}$ can be obtained by the Hamilton product between q_ω , the quaternion representation of the rotation matrix, and q_t . Compared to the integration approximation in prior work that violates the quaternion constraint of \mathcal{S}^3 (Supplementary E), integration by Eq. 3 and Eq. 4 ensures an exact quaternion solution at all times, leading to more accurate estimations, as demonstrated via the ablation in Tab. 3.

3.3 META-PD CONTROLLER WITH SECOND-ORDER ACCELERATION

The *ordinary differential equation* (ODE) that describes the motion acceleration $\dot{\omega}_t$ is written as

$$\dot{\omega}_t = \underbrace{\kappa_P(\text{vec}(\hat{q}_t \otimes q_t^*)) - \kappa_D \omega_t}_{\text{meta-PD algorithm}} + \underbrace{b_t}_{\text{bias}} + \underbrace{\kappa_A(\text{vec}(\hat{q}_t \otimes \hat{q}_{t-\Delta t}^*) - \text{vec}(\hat{q}_{t-\Delta t} \otimes \hat{q}_{t-2\Delta t}^*))}_{\text{acceleration enhancement}}, \quad (5)$$

where $\kappa_P \in \mathbb{R}$ and $\kappa_D \in \mathbb{R}$ constitute the PD controller’s proportional-derivative gains, while $\kappa_A \in \mathbb{R}$ is the scaling factor of the newly introduced second-order acceleration. The control signals b_t , κ_P , κ_D , κ_A are predicted by a *ControlNet* via linear projections from the latent embedding, given q_t , ω_t and \hat{q}_t as inputs (Fig. 2). Inspired by Fresk & Nikolakopoulos (2013), the meta-PD controller is computed proportionally to the vector, *i.e.* imaginary, part of the quaternion error between \hat{q}_t and the complex conjugate of q_t , q_t^* . Due to the online setting considered in our work, the estimated \hat{q}_t is inherently noisy, especially when obtained from a direct regression method such as Sun et al. (2023). We suggest the derivative term $\kappa_D \omega_t$ to dampen the predicted proportional control signal $\kappa_P(\text{vec}(\hat{q}_t \otimes q_t^*))$, effectively reducing overshooting and jittery. The data-driven b_t is the estimation of f_ω approximated from the embedding of *ControlNet*, commonly referred as bias term in prior work (Shimada et al., 2020; Li et al., 2022a).

The proposed **acceleration enhancement** term is the best guess of the person’s intended target pose, computed from the second-order quaternion difference of the last three reference poses $\hat{q}_{t-2\Delta t:t}$, resulting in the angular acceleration of the reference signal. This term, scaled by κ_A , reacts adaptively to the rate of change in reference signals, *i.e.*, it positively reinforces the controller when the reference \hat{q} changes fast (quick movements to reach a new target) and dampens the control signals as the motion moves closer to the target. The adaptive nature of the acceleration enhancement helps the kinematics motion react quickly to the intended target, while maintaining minimal overshooting.

Global translation. We also compute the root translation r_t with meta-PD and Euler integration (Li et al., 2022a). The calculation is written as: $r_{t+\Delta t} = r_t + (v_t + (\kappa_P(\hat{r}_t - r_t) - \kappa_D v_t)\Delta t)\Delta t$, with \hat{r}_t as the reference root position and v_t as the current root linear velocity. The global motion trajectory is then obtained by adding the translation r_t to the body mesh m_t or keypoints p_t respectively. A stability analysis of global translation can be found in Supplementary F.

3.4 TRAINING OBJECTIVES

The total objective $\mathcal{L}_{\text{total}}$ for capturing 3D human motion consists of three different loss terms, defined in Eq. 6. The first loss is the local reconstruction loss $\mathcal{L}_{\text{local}}$, which is the frame-wise L1 distance between the predicted root-aligned 3D keypoint p_t to the ground truth p_t^{GT} from the respective dataset. The same calculation applies to the root translation r_t . The second loss is the

global consistency loss $\mathcal{L}_{\text{global}}$, which is the average L1 distance between second-order finite differences of the predicted motion $p_{1:T}$ and ground truth $p_{1:T}^{GT}$. The finite differences are computed as $\ddot{x}_{0:T} = x_{0:T-2} - 2x_{1:T-1} + x_{2:T}$, with x being either p or r . We additionally fine-tune the shape parameter β via a learnable β_{fix} . To prevent unrealistic body shapes, we introduce a regularization on β_{fix} , ensuring the estimated body shapes do not deviate far from the average human shape ($\beta = 0$).

$$\begin{aligned}\mathcal{L}_{\text{total}} &= \mathcal{L}_{\text{local}} + \mathcal{L}_{\text{global}} + \lambda \mathcal{L}_{\text{beta}}, \quad \mathcal{L}_{\text{beta}} = \|\beta_{\text{fix}}\|, \\ \mathcal{L}_{\text{local}} &= \frac{1}{T} \frac{1}{N} \sum_{t=1}^T \sum_{n=1}^N |p_{0:T}^{GT} - p_{0:T}| + \frac{1}{T} \sum_{t=1}^T |r_{0:T}^{GT} - r_{0:T}|, \\ \mathcal{L}_{\text{global}} &= \frac{1}{T} \frac{1}{N} \sum_{t=1}^T \sum_{n=1}^N |\ddot{p}_{0:T}^{GT} - \ddot{p}_{0:T}| + \frac{1}{T} \sum_{t=1}^T |\ddot{r}_{0:T}^{GT} - \ddot{r}_{0:T}|.\end{aligned}\quad (6)$$

4 EXPERIMENTS

4.1 DATASETS

We evaluate QuaMo on four established motion capture datasets. The main dataset in comparison with related methods is Human3.6M (Ionescu et al., 2014). The dataset contains diverse human motion capture data from seven actors in a laboratory setup. Following prior work (Shimada et al., 2021; Yuan et al., 2021; Le et al., 2024a), data from the first five actors (S1, S5, S6, S7, S8) is used for training, while S9 and S11 are reserved for testing. For a fair comparison, as suggested by Shimada et al. (2021), only actions that involve foot-ground contacts are considered. To demonstrate the performance of our method on more diverse motions, we additionally evaluate on the Fit3D (Fieraru et al., 2021) and SportsPose dataset (Ingwersen et al., 2023). The former contains complex exercise motions with a laboratory setup similar to Human3.6M. The latter comprises sport action videos taken with a mobile phone in different scene setups. We employ the training split from Le et al. (2024a) for evaluation. Lastly, following Gäßtner et al. (2022a), we test QuaMo on a subset of AIST (Li et al., 2021b) (details in Supplementary C), consisting of dancing videos with pseudo ground-truths from 3D triangulation.

4.2 IMPLEMENTATION DETAILS

QuaMo is implemented as an online end-to-end approach as in Fig. 2. At time step t , the system states q_t , ω_t and target pose \hat{q}_t are used as inputs for the ControlNet, followed by two heads for κ_P and κ_D , one head for data-driven bias b_t , and one head for κ_A predictions of Eq. 5. The target poses \hat{q} are initially extracted using TRACE (Sun et al., 2023) and HMR2.0 (Goel et al., 2023). Following (Shimada et al., 2021; Gäßtner et al., 2022a; Le et al., 2024a), the extracted motions are down-sampled from 50Hz to 25Hz, first frame prediction root-aligned to the world origin, and then split into sub-sequences of 100 frames for batch training. The estimated pose q is in SMPL format and uses a mesh-based linear regression to obtain the keypoint predictions. In addition to the ControlNet, we create an InitNet for creating the initial states q_0 , ω_0 and β_{fix} , taking only the first two target poses $\hat{q}_{0:1}$, and the first shape parameter β_0 (from either TRACE or HMR2.0) as inputs. Please refer to Supplementary A for details about InitNet and ControlNet.

For all experiments, QuaMo is trained for a total of 35 epochs with a batch size of 64 and an initial learning rate of $5e^{-4}$, with an exponential decay at epoch 20 and 30 by a factor of 10. The ControlNet consists of two fully connected layers with a hidden dimension of 512, followed by a *LayerNorm* and *LeakyReLU* activation. To stabilize the training in the beginning, in the first 5 epochs, the network parameters are updated per-frame with a learning rate of $1e^{-4}$ while the global loss $\mathcal{L}_{\text{global}}$ is turned off. During training, the shape loss $\mathcal{L}_{\text{beta}}$ is scaled by $\lambda = 0.01$. The time step $\Delta t = 0.04$ corresponds to the down-sampled motion capture rate of 25Hz. All experiments are reported with error bars obtained by testing on five different random seed values (0 – 4).

4.3 METRICS

We evaluate QuaMo on all of the datasets with two set of metrics: local and global. The local metrics consider the Mean Per Joint Position Error (MPJPE) (in mm) between root-aligned poses.

Method	Tmpl.	Kin.	Onl.	Local metrics			Global metrics			
				MPJPE	P-MPJPE	Accel	G-MPJPE	GRE	G-Accel	FS
PoseAnchor (Kim et al., 2025)	-	-	-	40.3	32.1	-	-	-	-	-
KTPFormer (Peng et al., 2024)	-	-	-	40.1	31.9	-	-	-	-	-
PoseMamba (Huang et al., 2025)	-	-	-	37.1	31.5	-	-	-	-	-
Mambapose (Lang & Chuah (2025)	-	-	-	36.5	28.6	-	-	-	-	-
HMMR (Kanazawa et al., 2019)	✓	-	-	79.4	55.0	-	-	231.1	-	-
VIBE (Kocabas et al., 2020)	✓	-	-	68.6	43.6	23.4	207.7	-	-	27.4
MAED (Wan et al., 2021)	✓	-	-	56.4	38.7	-	-	-	-	-
HMR (Kanazawa et al., 2018)	✓	-	✓	78.9	54.3	-	-	204.2	-	-
IPMAN-R (Tripathi et al., 2023)	✓	-	✓	60.7	41.1	-	-	-	-	-
TRACE (Sun et al., 2023)	✓	-	✓	56.1	39.4	18.9	143.0	127.2	39.4	80.3
HybRIK (Li et al., 2021a)	✓	-	✓	55.4	33.6	-	-	-	-	-
MeshPose (Le et al., 2024b)	✓	-	✓	50.7	35.4	-	-	-	-	-
HMR2.0 (Goel et al., 2023)	✓	-	✓	46.7	30.7	9.1	97.2	86.8	16.8	11.5
PhysCap (Shimada et al., 2020)	✓	✓	-	97.4	65.1	-	-	182.6	-	-
TrajOpt (Gärtner et al., 2022b)	✓	✓	-	84.0	56.0	-	143.0	-	-	4.0
DiffPhy (Gärtner et al., 2022a)	✓	✓	-	81.7	55.6	-	139.1	-	-	7.4
Xie et al. (2021)	✓	✓	-	68.1	-	-	-	85.1	-	-
PhysPT (Zhang et al., 2024)	✓	✓	-	52.7	36.7	2.5	335.7	-	-	-
DnD (Li et al., 2022a)	✓	✓	-	52.5	35.5	-	525.3	-	-	-
NeurPhys (Shimada et al., 2021)	✓	✓	✓	76.5	58.2	-	-	-	-	-
SimPoE (Yuan et al., 2021)	✓	✓	✓	56.7	41.6	6.7	-	-	-	-
OSDCap (Le et al., 2024a)	✓	✓	✓	54.8	39.8	8.4	132.8	119.1	16.0	15.2
QuaMo_TRACE (Ours)	✓	✓	✓	51.3 ± 0.11	37.5 ± 0.05	5.7 ± 0.03	116.2 ± 1.04	101.4 ± 1.37	7.8 ± 0.06	6.6 ± 1.78
QuaMo_HMR2.0 (Ours)	✓	✓	✓	46.7 ± 0.04	30.6 ± 0.03	5.3 ± 0.04	88.8 ± 0.21	78.5 ± 0.33	6.8 ± 0.07	4.3 ± 0.04

Table 1: Quantitative results on the Human3.6M dataset (Ionescu et al., 2014). Tmpl.: Template-based approach (*i.e.* SMPL-based). Kin.: kinematics-based approach. Onl.: online approach. Online methods work with only one future target pose at each time step. **Bold** highlights the best results within the kinematics category. The proposed QuaMo reaches state-of-the-art performance on the MPJPE, P-MPJPE, G-MPJPE, and GRE with HMR2.0 as the meta-PD controller target. On the motion plausibly metrics Accel, G-Accel, FS, we consistently record better results compared to other online kinematics-based approaches.

The MPJPE calculates the average frame-wise L2 distance between estimated human joint 3D coordinates and the ground truth data. The second metric, P-MPJPE, is MPJPE with a rigid alignment between two poses. To evaluate the motion jitter, we consider the Accel metric (mm/frame²), which measures the difference between the predicted joint acceleration and the ground truth. In addition, motion artifacts can only be observed in a world coordinate with global translation (Gärtner et al., 2022a). The G-MPJPE computes MPJPE in global coordinates without root alignment. We also compute the Global Root Error (GRE), similar to MPJPE, but only on root translation. The global jitter G-Accel is computed similarly to Accel without root alignment. Foot skating (FS) is measured as the percentage (%) of frames that contain foot movements more than 2cm during contact.

4.4 RESULTS

We report the quantitative evaluation results of QuaMo in Tab. 1, with comparison to five groups of related study: 1) keypoint-based approaches that lifted from 2D keypoints (Peng et al., 2024; Sun et al., 2024; Lang & Chuah, 2025; Huang et al., 2025; Kim et al., 2025), 2) vision-based approaches that utilize temporal information (Kanazawa et al., 2019; Kocabas et al., 2020; Wan et al., 2021), 3) single-or-two-frame prediction only (Kanazawa et al., 2018; Tripathi et al., 2023; Li et al., 2021a; Sun et al., 2023; Goel et al., 2023), 4) kinematics-based methods that base their prediction on a large window of frames (Li et al., 2022a; Zhang et al., 2024) or trajectory-optimization methods (Shimada et al., 2020; Gärtner et al., 2022b;a; Xie et al., 2021), and most related to our work, 5) kinematics-based online methods that only consider two frames as input (Shimada et al., 2021; Yuan et al., 2021; Le et al., 2024a). The methods are ranked with respect to their performance on the MPJPE

Data	Method	MPJPE	P-MPJPE	Accel	G-MPJPE	GRE	G-Accel	FS
Fit3D	TRACE (Sun et al., 2023)	63.9	43.8	19.1	111.3	83.2	42.4	87.5
	OSDCap (Le et al., 2024a)	58.7	42.6	8.2	73.8	47.2	12.8	25.9
	QuaMo_TRACE (Ours)	50.3 _{±0.13}	35.6 _{±0.04}	3.8 _{±0.01}	68.8 _{±0.21}	45.2 _{±0.15}	5.6 _{±0.03}	16.3 _{±0.27}
Sports-Pose	TRACE (Sun et al., 2023)	99.3	68.7	14.7	421.7	389.1	39.1	38.5
	OSDCap (Le et al., 2024a)	71.7	52.4	10.9	113.6	90.2	17.1	38.0
	QuaMo_TRACE (Ours)	71.4 _{±0.30}	48.7 _{±0.21}	5.3 _{±0.19}	112.2 _{±0.75}	82.3 _{±0.36}	13.7 _{±0.13}	24.1 _{±0.91}
AIST	TRACE (Sun et al., 2023)	115.6	63.2	34.1	243.8	208.3	107.5	104.4
	HUND (Zanfir et al., 2021)	107.4	66.9	-	155.7	-	-	50.9
	DiffPhy (Gärtner et al., 2022a)	105.5	66.0	-	150.2	-	-	19.6
	HMR2.0 (Goel et al., 2023)	101.9	60.2	24.4	154.3	110.5	40.7	56.0
	QuaMo_HMR2.0 (Ours)	89.1 _{±0.14}	60.0 _{±0.20}	14.7 _{±0.02}	144.1 _{±0.57}	108.7 _{±1.07}	14.9 _{±0.07}	13.0 _{±0.46}

Table 2: Quantitative results on the Fit3D (Fieraru et al., 2021) (top), SportsPose (Ingwersen et al., 2023) (middle) and the AIST (Li et al., 2021b) (bottom) dataset. Compared to OSDCap (Le et al., 2024a), QuaMo achieves a better performance on Fit3D and SportsPose, especially on the jittery metrics, using the same input TRACE. On AIST, with HMR2.0 as input, the proposed online QuaMo outperforms an offline method, DiffPhy, on both pose accuracy and motion jitter.

metric, within their respective category. Keypoint-based methods are only presented for referencing purposes and cannot be compared to template-based methods.

The proposed QuaMo is evaluated using two different online approaches: TRACE (Sun et al., 2023) and HMR2.0 (Goel et al., 2023) as the references for the PD controller. TRACE (Sun et al., 2023) directly regresses the 3D SMPL pose from input images, resulting in noisy 3D estimation with an Accel of 18.9 and FS of 80.3%. Using QuaMo, we manage to improve not only Accel and FS, but also MPJPE by 8.6%, P-MPJPE by 5.1%, and G-MPJPE by 18.7%. While TRACE is used for a fair comparison to competitors, we further improve the performance by using the newer HMR2.0 for the PD controller targets, which achieves state-of-the-art results on MPJPE, P-MPJPE, and G-MPJPE across all categories, while producing more plausible motions compared to other online methods. The improvement compared to HMR2.0 on Accel is 41.8%, 59.5% on G-Accel, and 62.6% in FS.

Our direct competitor is OSDCap (Le et al., 2024a), which is also an online dynamics-based approach. We outperform OSDCap on every metric, while using the same PD controller’s target as TRACE (Sun et al., 2023): notably, 6.3% on MPJPE, 32.1% on Accel, and 12.5% on G-MPJPE. OSDCap, despite achieving a good state estimation through a Kalman-filter approach, re-introduces implausibility from the inputs obtained by TRACE back to the final output. We, however, achieve much smoother and plausible motions by fully respecting the temporal relationship between consecutive predictions from the integration scheme. DnD (Li et al., 2022a) and PhysPT (Zhang et al., 2024), despite having a competitive performance, take a window of 16 frames as input, while ours only takes one next frame as target. PhysPT (Zhang et al., 2024) achieves a smoother motion than our QuaMo; however, their motion is reconstructed from a seq2seq transformer model (Vaswani et al., 2017), without having an integration scheme to ensure temporal dependency between consecutive frame predictions. TrajOpt (Gärtner et al., 2022b) has a better FS measurement due to their offline trajectory optimization approach with a global refinement, whereas QuaMo is fully online and still maintains a competitive FS of 4.3% (compared to 4.0% of TrajOpt) with much lower MPJPE.

While the Human3.6M dataset serves as a baseline for benchmarking human pose estimation approaches, the variability of motions in the dataset is limited. Therefore, we also conduct an evaluation on the Fit3D (Fieraru et al., 2021) and SportsPose (Ingwersen et al., 2023) datasets with more complex and more challenging sports movements, presented in Tab. 2. Similar to the results in Tab. 1, we improve upon the input TRACE by a large margin and outperform OSDCap on all metrics. Additionally, we follow DiffPhy (Gärtner et al., 2022a) and evaluate QuaMo on the same subset of the AIST database (Li et al., 2021b), shown in Tab. 2. Because the implementation of HUND (Zanfir et al., 2021), the target input of DiffPhy, is not publicly available, we use HMR2.0 as our PD target instead. QuaMo achieves better results on all accuracy and plausibility metrics. Some qualitative results showing the advantage of QuaMo are presented in Fig. 3. Additional visualizations can be found in Supplementary B and videos on our supplemental webpage.

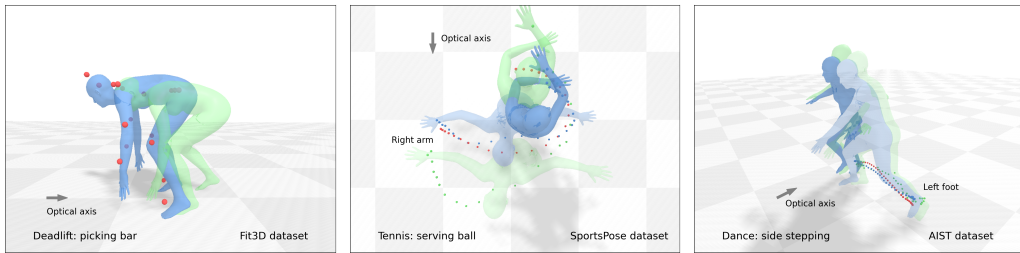


Figure 3: Qualitative results on three datasets: Fit3D (left), SportsPose (middle), AIST (right). QuaMo’s predictions are shown in blue, the input (from TRACE or HMR2.0) in green, and ground truth keypoints in red for reference. The start frame has lower transparency. The reconstructed motions from QuaMo have significantly lower jitter and higher accuracy along the optical axis.

Method	Rotation	f_ω	\mathcal{S}^3	α	MPJPE	P-MPJPE	Accel	G-MPJPE	G-Accel	FS
TRACE	Axis-angle	-	-	-	56.3	39.3	19.3	146.4	44.5	80.3
PD only	Euler XYZ	-	-	-	74.4 ± 3.86	39.7 ± 0.84	13.7 ± 2.02	148.7 ± 3.71	15.4 ± 1.91	17.3 ± 2.38
PD only	Euler ZXY	-	-	-	71.2 ± 2.17	41.1 ± 0.71	7.6 ± 1.02	143.9 ± 2.76	9.3 ± 0.92	19.7 ± 2.18
PD only	Axis-angle	-	-	-	60.6 ± 1.40	39.0 ± 0.14	6.4 ± 0.99	137.8 ± 1.32	8.2 ± 0.93	17.2 ± 0.93
PD only	Quaternion	-	-	-	53.8 ± 0.18	38.8 ± 0.15	5.7 ± 0.07	132.6 ± 3.22	7.9 ± 0.94	19.5 ± 1.23
QuaMo	Quaternion	✓	-	-	53.1 ± 0.05	38.6 ± 0.04	5.3 ± 0.03	115.9 ± 0.08	8.6 ± 0.12	13.9 ± 0.57
QuaMo	Quaternion	✓	✓	-	52.0 ± 0.07	38.1 ± 0.05	5.2 ± 0.02	114.8 ± 0.82	7.8 ± 0.09	10.6 ± 0.30
QuaMo	Quaternion	✓	✓	✓	51.3 ± 0.08	37.4 ± 0.04	5.9 ± 0.02	114.7 ± 1.01	8.4 ± 0.04	10.0 ± 0.30

Table 3: Ablation studies. The baseline uses only a PD controller (PD only), taking TRACE as targets. The f_ω : using the data-driven bias in Eq. 5; \mathcal{S}^3 : using the integration method from Eq. 3 and Eq. 4; α : using the acceleration enhancement term in Eq. 5. The model configurations are ranked based on their MPJPE score, and the lowest MPJPE with a reasonable Accel is most desired.

4.5 ABLATION STUDIES

We conduct two ablations in Tab. 3 to verify the usage of our proposals: using the quaternion as joint representation, and using the quaternion \mathcal{S}^3 constraint for integration and the acceleration enhancement. To reduce computational load, all ablations are conducted on a subset of Human3.6M taken from camera 60457274. Methods with lower MPJPE are more desirable. TRACE is chosen as the baseline and is presented in the first row of Tab. 3 for comparisons.

Joint rotation. We first compare the common joint representations: Axis-angle, Euler ZXY, Euler XYZ, and quaternion (ours), in row 2 to 5 in Tab. 3. As described in Sec. 1, axis-angle and Euler angles suffer from discontinuities over all three angles, causing instability during integration. An example is shown in Fig 4, when the temporally consistent human reconstruction has to make a full 180-degree rotation when the root joint encounters a discontinuity. This situation can be easily avoided by using quaternions. The experimental result of Euler angles in Tab. 3 shows that while having a reasonable MPJPE, the Accel is significantly larger, due to the constant compensation that the model has to produce to overcome the angle discontinuity. The axis-angle representation is more robust to the discontinuity; however, the error between two axis-angles for the PD controller cannot be defined in a physically meaningful way. We instead apply finite differences between each of the three components of the axis-angles separately as the error. As demonstrated with relevant metrics in Tab. 3, it is more difficult to correctly capture the motions with axis-angles than with quaternions.

QuaMo’s components. We gradually add the proposed solution to the baseline with quaternion rotation. The data-driven f_ω helps address the database-specific offsets that ensure accurate estimation, especially the global translation with G-MPJPE decreases from 132.6 to 115.9 mm. The quaternion integration with the spherical constraint \mathcal{S}^3 reduces the error of the QDE solving process, leading to a decrement from 53.1 to 52.0 mm in MPJPE. The proposed acceleration enhancement term with its adaptive ability further improves the estimation accuracy, with an MPJPE decrease from 52.0 to 51.3 mm. A trade-off of the acceleration term is the motion jitter (Accel increases from 5.2 to 5.9) due to the noise amplification from the second-order differences of the input TRACE. Despite the jittery

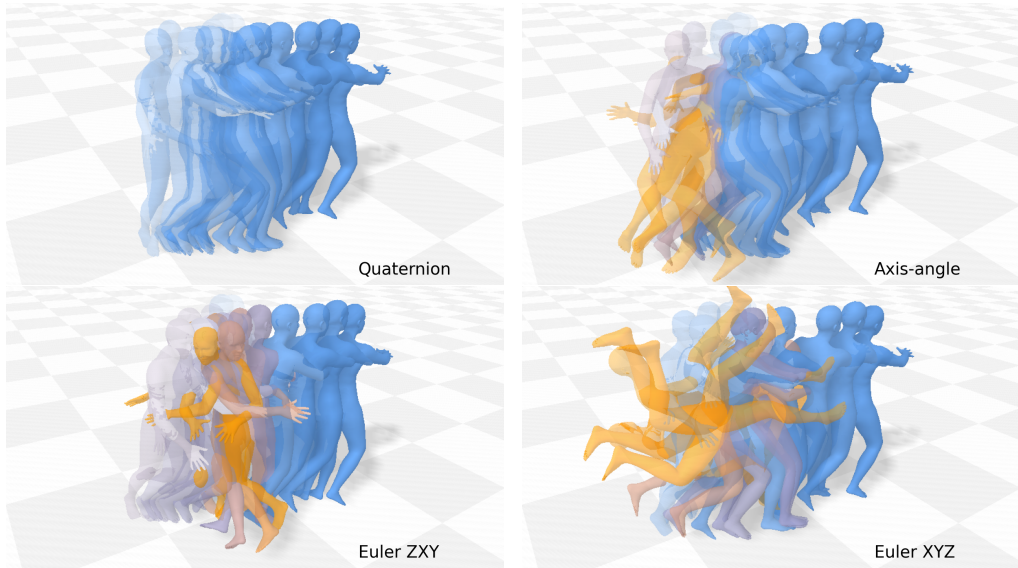


Figure 4: An example of motion reconstruction when a discontinuity occurs in the root joint rotation for different rotation representations. **Blue** means low and **orange** high MPJPE. The transparency corresponds to the time steps in the sequence. The model attempts to compensate for the discontinuity by rotating along the different rotation axes for all representations, except our quaternions.

trade-off, our proposed method enables accurate estimations for real-time downstream applications. The computational complexity of QuaMo is presented in Supplementary D.

Besides the training hyper-parameters taken from previous work OSDCap Le et al. (2024a) such as the same batch size 64, learning rate $5e-4$, hidden dimension 512, and the usage of LayerNorm and LeakyReLU activations; we additionally provide an ablation study on the choice of shape loss scaling factor λ in Tab 4. Because the Accel between different λ are similar, we choose $\lambda = 0.01$ as our final selection due to the good trade-off between the local MPJPE and the global G-MPJPE.

λ	MPJPE	G-MPJPE	Accel
1.0	52.8	120.2	5.8
0.1	51.8	118.6	5.8
0.01	51.2	116.2	5.7
0.001	51.0	116.9	5.7
0.0	51.1	117.1	5.7

Table 4: Ablation study on the shape loss scaling λ . We choose $\lambda = 0.01$ as our final selection due to the good performance trade-off between the local MPJPE and the global G-MPJPE.

5 CONCLUSION

In this paper, we introduce QuaMo, a novel online vision-based human kinematics capture method for recovering plausible human motions from cameras. Prior works often make use of Euler angles as the joint representation, which creates inaccurate solutions due to discontinuity during temporal integration. We propose the usage of the quaternion differential equation together with unit-sphere constrained solutions and acceleration enhancements for accurate and plausible 3D kinematics capture. We evaluate QuaMo in comparison with related work and achieve state-of-the-art results on four datasets: Human3.6M, Fit3D, SportsPose and AIST.

Limitation and future work. While human kinematics can be accurately estimated with QuaMo, the influence of the surrounding environment on the velocity predictions has the potential to further improve the plausibility of the reconstructed motions. As a natural extension, contacts and interactions of humans with external scenes will be investigated in future work.

ACKNOWLEDGMENTS AND DISCLOSURE OF FUNDING

This research is partially supported by the Wallenberg Artificial Intelligence, Autonomous Systems and Software Program (WASP), funded by Knut and Alice Wallenberg Foundation. The computational resources were provided by the National Academic Infrastructure for Supercomputing in Sweden (NAIIS) at C3SE, and by the Berzelius resource, provided by the Knut and Alice Wallenberg Foundation at the National Supercomputer Centre.

REFERENCES

Mazen Al Borno, Martin de Lasa, and Aaron Hertzmann. Trajectory optimization for full-body movements with complex contacts. *IEEE Transactions on Visualization and Computer Graphics*, 19(8):1405–1414, 2013.

Philipp Allgeuer and Sven Behnke. Fused angles and the deficiencies of euler angles. In *International Conference on Intelligent Robots and Systems (IROS)*, 2018.

Michael S. Andrlé and John L. Crassidis. Geometric integration of quaternions. *Journal of Guidance, Control, and Dynamics*, 36(6):1762–1767, 2013. doi: 10.2514/1.G000277.

Fabien Baradel, Matthieu Armando, Salma Galaaoui, Romain Brégier, Philippe Weinzaepfel, Grégoire Rogez, and Thomas Lucas. Multi-hmr: Multi-person whole-body human mesh recovery in a single shot. In *ECCV*, 2024.

Antonie J. van den Bogert, Thomas Geijtenbeek, Oshri Even-Zohar, Frans Steenbrink, and Elizabeth C. Hardin. A real-time system for biomechanical analysis of human movement and muscle function. *Medical and Biological Engineering and Computing*, 51:1069–1077, 2013.

Qingyuan Cai, Xuecai Hu, Saihui Hou, Li Yao, and Yongzhen Huang. Disentangled diffusion-based 3d human pose estimation with hierarchical spatial and temporal denoiser. In *AAAI*, volume 38, pp. 882–890, 2024.

Ricky T. Q. Chen, Yulia Rubanova, Jesse Bettencourt, and David Duvenaud. Neural ordinary differential equations. In *NeurIPS*, 2018.

Erwin Coumans and Yunfei Bai. Pybullet, a python module for physics simulation for games, robotics and machine learning. <http://pybullet.org>, 2016–2019.

Sai Kumar Dwivedi, Yu Sun, Priyanka Patel, Yao Feng, and Michael J. Black. TokenHMR: Advancing human mesh recovery with a tokenized pose representation. In *CVPR*, 2024.

Mihai Fieraru, Mihai Zanfir, Silviu-Cristian Pirlea, Vlad Olaru, and Cristian Sminchisescu. Aifit: Automatic 3d human-interpretable feedback models for fitness training. In *CVPR*, June 2021.

Emil Fresk and George Nikolakopoulos. Full quaternion based attitude control for a quadrotor. In *European Control Conference (ECC)*, 2013.

Shubham Goel, Georgios Pavlakos, Jathushan Rajasegaran, Angjoo Kanazawa, and Jitendra Malik. Humans in 4D: Reconstructing and tracking humans with transformers. In *ICCV*, 2023.

Michał Gołąbek, Michał Welcer, Cezary Szczępański, Mariusz Krawczyk, Albert Zajdel, and Krystian Borodacz. Quaternion attitude control system of highly maneuverable aircraft. *Electronics*, 11(22), 2022. ISSN 2079-9292. doi: 10.3390/electronics11223775.

Erik Gärtner, Mykhaylo Andriluka, Erwin Coumans, and Cristian Sminchisescu. Differentiable dynamics for articulated 3d human motion reconstruction. In *CVPR*, pp. 13190–13200, 2022a.

Erik Gärtner, Mykhaylo Andriluka, Hongyi Xu, and Cristian Sminchisescu. Trajectory optimization for physics-based reconstruction of 3d human pose from monocular video. In *CVPR*, pp. 13106–13115, 2022b.

Buzhen Huang, Liang Pan, Yuan Yang, Jingyi Ju, and Yangang Wang. Neural mocon: Neural motion control for physically plausible human motion capture. In *CVPR*, pp. 6417–6426, 2022.

Yunlong Huang, Junshuo Liu, Ke Xian, and Robert Caiming Qiu. Posemamba: Monocular 3d human pose estimation with bidirectional global-local spatio-temporal state space model. In *AAAI*, volume 39, pp. 3842–3850, 2025.

Christian Keilstrup Ingwersen, Christian Mikkelstrup, Janus Nørtoft Jensen, Morten Rieger Han-nemose, and Anders Bjørholm Dahl. Sportspose: A dynamic 3d sports pose dataset. In *IEEE/CVF International Workshop on Computer Vision in Sports*, 2023.

Catalin Ionescu, Dragos Papava, Vlad Olaru, and Cristian Sminchisescu. Human3.6m: Large scale datasets and predictive methods for 3d human sensing in natural environments. *IEEE TPAMI*, 36(7):1325–1339, 2014.

Angjoo Kanazawa, Michael J. Black, David W. Jacobs, and Jitendra Malik. End-to-end recovery of human shape and pose. In *CVPR*, 2018.

Angjoo Kanazawa, Jason Y. Zhang, Panna Felsen, and Jitendra Malik. Learning 3d human dynamics from video. In *CVPR*, June 2019.

Jeonghwan Kim, Mi-Gyeong Gwon, Hyunwoo Park, Hyukmin Kwon, Gi-Mun Um, and Wonjun Kim. Sampling is Matter: Point-guided 3d human mesh reconstruction. In *CVPR*, June 2023.

Jun-Hee Kim, Jumin Han, and Seong-Whan Lee. Poseanchor: Robust root position estimation for 3d human pose estimation. In *ICCV*, pp. 7079–7088, 2025.

Muhammed Kocabas, Nikos Athanasiou, and Michael J. Black. Vibe: Video inference for human body pose and shape estimation. In *CVPR*, pp. 5253–5263, 2020.

Jack B Kuipers. *Quaternions and rotation sequences: a primer with applications to orbits, aerospace, and virtual reality*. Princeton university press, 1999.

Bo Lang and Mooi Choo Chuah. Event-guided fusion-mamba for context-aware 3d human pose estimation. In *WACV*, pp. 950–960, February 2025.

Cuong Le, Viktor Johannson, Manon Kok, and Bastian Wandt. Optimal-state dynamics estimation for physics-based human motion capture from videos. In *NeurIPS*, 2024a.

Eric-Tuan Le, Antonis Kakolyris, Petros Koutras, Himmy Tam, Efstratios Skordos, George Papan-dreou, Riza Alp Güler, and Iasonas Kokkinos. Meshpose: Unifying densepose and 3d body mesh reconstruction. In *CVPR*, pp. 2405–2414, June 2024b.

Jiefeng Li, Chao Xu, Zhicun Chen, Siyuan Bian, Lixin Yang, and Cewu Lu. Hybrik: A hybrid analytical-neural inverse kinematics solution for 3d human pose and shape estimation. In *CVPR*, pp. 3383–3393, 2021a.

Jiefeng Li, Siyuan Bian, Chao Xu, Gang Liu, Gang Yu, and Cewu Lu. D&d: Learning human dynamics from dynamic camera. In *ECCV*, 2022a.

Ruilong Li, Shan Yang, David A. Ross, and Angjoo Kanazawa. Ai choreographer: Music conditioned 3d dance generation with aist++. In *ICCV*, pp. 13401–13412, October 2021b.

Shichao Li, Lei Ke, Kevin Pratama, Yu-Wing Tai, Chi-Keung Tang, and Kwang-Ting Cheng. Cascaded deep monocular 3d human pose estimation with evolutionary training data. In *CVPR*, 2020.

Zhihao Li, Jianzhuang Liu, Zhensong Zhang, Songcen Xu, and Youliang Yan. Cliff: Carrying location information in full frames into human pose and shape estimation. In *ECCV*, 2022b.

Tsung-Yi Lin, Michael Maire, Serge Belongie, Lubomir Bourdev, Ross Girshick, James Hays, Pietro Perona, Deva Ramanan, Piotr Dollár, and C Lawrence Zitnick. Microsoft coco: Common objects in context. In *ECCV*, 2014.

Matthew Loper, Naureen Mahmood, Javier Romero, Gerard Pons-Moll, and Michael J. Black. SMPL: A skinned multi-person linear model. *ACM TOG*, 34(6):248:1–248:16, October 2015.

Naureen Mahmood, Nima Ghorbani, Nikolaus F. Troje, Gerard Pons-Moll, and Michael J. Black. AMASS: Archive of motion capture as surface shapes. In *ICCV*, pp. 5442–5451, October 2019.

Priyanka Patel and Michael J. Black. Camerahmr: Aligning people with perspective. In *International Conference on 3D Vision (3DV)*, 2025.

Georgios Pavlakos, Xiaowei Zhou, Konstantinos G. Derpanis, and Kostas Daniilidis. Coarse-to-fine volumetric prediction for single-image 3d human pose. In *CVPR*, July 2017.

Georgios Pavlakos, Vasileios Choutas, Nima Ghorbani, Timo Bolkart, Ahmed A. A. Osman, Dimitrios Tzionas, and Michael J. Black. Expressive body capture: 3d hands, face, and body from a single image. In *CVPR*, 2019.

Dario Pavllo, Christoph Feichtenhofer, David Grangier, and Michael Auli. 3d human pose estimation in video with temporal convolutions and semi-supervised training. In *CVPR*, 2019.

Jihua Peng, Yanghong Zhou, and PY Mok. Ktpformer: Kinematics and trajectory prior knowledge-enhanced transformer for 3d human pose estimation. In *CVPR*, pp. 1123–1132, 2024.

Xue Bin Peng, Yunrong Guo, Lina Halper, Sergey Levine, and Sanja Fidler. Ase: Large-scale reusable adversarial skill embeddings for physically simulated characters. *ACM TOG*, 41(4), 2022. ISSN 0730-0301.

Maria Priisalu, Ciprian Paduraru, Aleksis Pirinen, and Cristian Sminchisescu. Semantic synthesis of pedestrian locomotion. In *ACCV*, November 2020.

Davis Rempe, Leonidas J. Guibas, Aaron Hertzmann, Bryan Russell, Ruben Villegas, and Jimei Yang. Contact and human dynamics from monocular video. In *ECCV*, 2020.

Davis Rempe, Tolga Birdal, Aaron Hertzmann, Jimei Yang, Srinath Sridhar, and Leonidas J. Guibas. Humor: 3d human motion model for robust pose estimation. In *CVPR*, pp. 11488–11499, 2021.

Soshi Shimada, Vladislav Golyanik, Weipeng Xu, and Christian Theobalt. Physcap: Physically plausible monocular 3d motion capture in real time. *ACM TOG*, 39(6), 2020.

Soshi Shimada, Vladislav Golyanik, Weipeng Xu, Patrick Pérez, and Christian Theobalt. Neural monocular 3D human motion capture with physical awareness. *ACM TOG*, 40(4), 2021. ISSN 0730-0301.

Ken Shoemake. Animating rotation with quaternion curves. In *Annual Conference on Computer Graphics and Interactive Techniques, SIGGRAPH'85*, pp. 245–254, New York, NY, USA, 1985. Association for Computing Machinery. ISBN 0897911660. doi: 10.1145/325334.325242.

Yu Sun, Qian Bao, Wu Liu, Tao Mei, and Michael J. Black. TRACE: 5D Temporal Regression of Avatars with Dynamic Cameras in 3D Environments. In *CVPR*, 2023.

Ziming Sun, Yuan Liang, Zejun Ma, Tianle Zhang, Linchao Bao, Guiqing Li, and Shengfeng He. Repose: 3d human pose estimation via spatio-temporal depth relational consistency. In *ECCV*, volume 15077 of *Lecture Notes in Computer Science*, pp. 309–325. Springer, 2024.

Emanuel Todorov, Tom Erez, and Yuval Tassa. Mujoco: A physics engine for model-based control. In *2012 IEEE/RSJ International Conference on Intelligent Robots and Systems*, pp. 5026–5033, 2012.

Shashank Tripathi, Lea Müller, Chun-Hao P. Huang, Omid Taheri, Michael J. Black, and Dimitrios Tzionas. 3d human pose estimation via intuitive physics. In *CVPR*, pp. 4713–4725, June 2023.

Scott D. Uhlrich, Antoine Falisse, Łukasz Kidziński, Julie Muccini, Michael Ko, Akshay S. Chaudhari, Jennifer L. Hicks, and Scott L. Delp. Opencap: Human movement dynamics from smartphone videos. *PLOS Computational Biology*, 19(10):1–26, 10 2023.

Ashish Vaswani, Noam Shazeer, Niki Parmar, Jakob Uszkoreit, Llion Jones, Aidan N Gomez, Łukasz Kaiser, and Illia Polosukhin. Attention is all you need. In *NeurIPS*, volume 30, 2017.

Ziniu Wan, Zhengjia Li, Maoqing Tian, Jianbo Liu, Shuai Yi, and Hongsheng Li. Encoder-decoder with multi-level attention for 3d human shape and pose estimation. In *ICCV*, 2021.

Bastian Wandt and Bodo Rosenhahn. Repnet: Weakly supervised training of an adversarial reprojection network for 3d human pose estimation. In *CVPR*, June 2019.

Bastian Wandt, Marco Rudolph, Petriissa Zell, Helge Rhodin, and Bodo Rosenhahn. Canonpose: Self-supervised monocular 3d human pose estimation in the wild. In *CVPR*, 2021.

Jingbo Wang, Zhengyi Luo, Ye Yuan, Yixuan Li, and Bo Dai. Pacer+: On-demand pedestrian animation controller in driving scenarios. In *CVPR*, pp. 718–728, June 2024.

Jue Wang, Shaoli Huang, Xinchao Wang, and Dacheng Tao. Not all parts are created equal: 3d pose estimation by modelling bi-directional dependencies of body parts. In *ICCV*, 2019.

Yufu Wang and Kostas Daniilidis. Refit: Recurrent fitting network for 3d human recovery. In *ICCV*, 2023.

Kevin Xie, Tingwu Wang, Umar Iqbal, Yunrong Guo, Sanja Fidler, and Florian Shkurti. Physics-based human motion estimation and synthesis from videos. In *ICCV*, pp. 11532–11541, 2021.

Jingwei Xu, Zhenbo Yu, Bingbing Ni, Jiancheng Yang, Xiaokang Yang, and Wenjun Zhang. Deep kinematics analysis for monocular 3d human pose estimation. In *CVPR*, 2020.

Yaguang Yang. *Spacecraft modeling, attitude determination, and control: quaternion-based approach*. CRC Press, 2019.

Heyuan Yao, Zhenhua Song, Baoquan Chen, and Libin Liu. Controlvae: Model-based learning of generative controllers for physics-based characters. *ACM TOG*, 41(6), 2022. ISSN 0730-0301.

Yingxuan You, Hong Liu, Ti Wang, Wenhao Li, Runwei Ding, and Xia Li. Co-evolution of pose and mesh for 3d human body estimation from video. In *ICCV*, pp. 14963–14973, 2023.

Ri Yu, Hwangpil Park, and Jehee Lee. Human dynamics from monocular video with dynamic camera movements. *ACM TOG*, 40(6), 2021. ISSN 0730-0301.

Ye Yuan, Shih-En Wei, Tomas Simon, Kris Kitani, and Jason Saragih. Simpoe: Simulated character control for 3d human pose estimation. In *CVPR*, pp. 7159–7169, 2021.

Ye Yuan, Jiaming Song, Umar Iqbal, Arash Vahdat, and Jan Kautz. Physdiff: Physics-guided human motion diffusion model. In *ICCV*, pp. 16010–16021, October 2023.

Andrei Zanfir, Eduard Gabriel Bazavan, Mihai Zanfir, William T. Freeman, Rahul Sukthankar, and Cristian Sminchisescu. Neural descent for visual 3d human pose and shape. In *CVPR*, pp. 14484–14493, June 2021.

Yufei Zhang, Jeffrey O. Kephart, Zijun Cui, and Qiang Ji. Physpt: Physics-aware pretrained transformer for estimating human dynamics from monocular videos. In *CVPR*, pp. 2305–2317, June 2024.

Qitao Zhao, Ce Zheng, Mengyuan Liu, Pichao Wang, and Chen Chen. Poseformerv2: Exploring frequency domain for efficient and robust 3d human pose estimation. In *CVPR*, pp. 8877–8886, June 2023.

Ce Zheng, Sijie Zhu, Matias Mendieta, Taojiannan Yang, Chen Chen, and Zhengming Ding. 3d human pose estimation with spatial and temporal transformers. In *ICCV*, 2021.

Wentao Zhu, Xiaoxuan Ma, Zhaoyang Liu, Libin Liu, Wayne Wu, and Yizhou Wang. Motionbert: A unified perspective on learning human motion representations. In *ICCV*, 2023.

SUPPLEMENTARY MATERIAL

This supplementary document provides additional information about QuaMo. Sec. A contains the details about the two neural networks used in the project, InitNet and ControlNet. Sec. B provides additional qualitative results with corresponding 2D projections of QuaMo’s predictions on the original images. Sec. C contains details about the training samples for the experiments on AIST dataset. Sec. D presents the computational complexity of QuaMo, and Sec. E discusses the approximated quaternion integration from prior work.

A NETWORKS DESIGN

The overall design of ControlNet is shown in Fig. 5. At every time step t , the ControlNet takes in as inputs the current human pose $q_t \in \mathbb{R}^{24 \times 4}$, angular velocity $\omega_t \in \mathbb{R}^{24 \times 3}$, reference pose $\hat{q}_t \in \mathbb{R}^{24 \times 4}$, root translation $r_t \in \mathbb{R}^3$, root velocity $v_t \in \mathbb{R}^3$, and reference root translation $\hat{r}_t \in \mathbb{R}^3$. All variables are concatenated into a single input vector of shape \mathbb{R}^{273} . The input is passed through two blocks of a sequential module, including a linear projection to embed dimension of 512, followed by LayerNorm and LeakyReLU activation. The output embedding with shape \mathbb{R}^{512} is then linearly projected to respective components of the meta-PD controller with acceleration enhancement.

Since neural networks work more stably with small numbers, we scale up the prediction of the parameters $\kappa_A, \kappa_P, \kappa_D$ by s_A, s_P, s_D respectively. The sigmoid functions ensure that the prediction is positive and within the range of $[0, s]$, leading to correct PD calculation and a stable ODE solving process, especially at the beginning of training. The chosen values for the scales are $s_A = 40, s_P = 40, s_D = 30$. For root translation, the scales are $s_P = 200, s_D = 200$. We found that these values are sufficient to prevent the ODE solver instability during training.

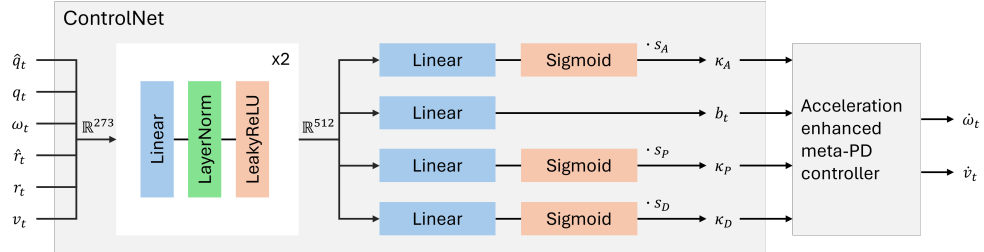


Figure 5: The architecture of ControlNet. The inputs are concatenated and linearly mapped to an embedding vector of 512 dimensions. The control parameters for the PD controller is predicted from the embedding via linear mappings, sigmoid functions and scaling.

To generate the initial solution for the QDE solvers, we implement an additional InitNet that takes in as input the first two reference poses $\hat{q}_{0:1}$, two reference root translations $\hat{r}_{0:1}$, and shape β_0 estimated from either TRACE or HMR2.0. The overall design of InitNet is shown in Fig. 6. QuaMo initial pose q_0 , translation r_0 , and SMPL shape β are directly learned from the inputs obtained from the 3D pose estimator. The shape β is kept constant throughout the whole 100-frame sequential integration of QuaMo. The initial angular velocity ω_0 and linear velocity v_0 are linearly mapped from the error between the first two reference poses $\hat{q}_1 \otimes \hat{q}_0^*$ and the first two root translations $\hat{r}_1 - \hat{r}_0$.

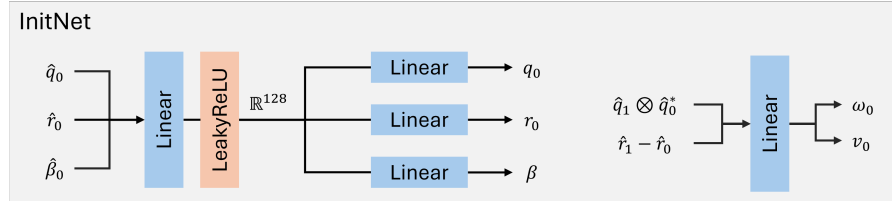


Figure 6: The architecture of InitNet. The initial solution of QuaMo is predicted based on the first two frames of the 3D pose estimator (TRACE or HMR2.0). To enforce the shape plausibility, β is kept constant throughout the sequence.

B ADDITIONAL RESULTS

In this section, we present additional qualitative results of QuaMo, together with the corresponding 2D projection on the input images. For each example presented in Fig. 7, the input image is on the left, 3D motion estimation is on the right, and the projected 2D poses are obtained with the provided intrinsic matrix from their respective datasets. For more insights into QuaMo, we encourage the reader to have a look at our videos that can be viewed by accessing the *index.html* file.

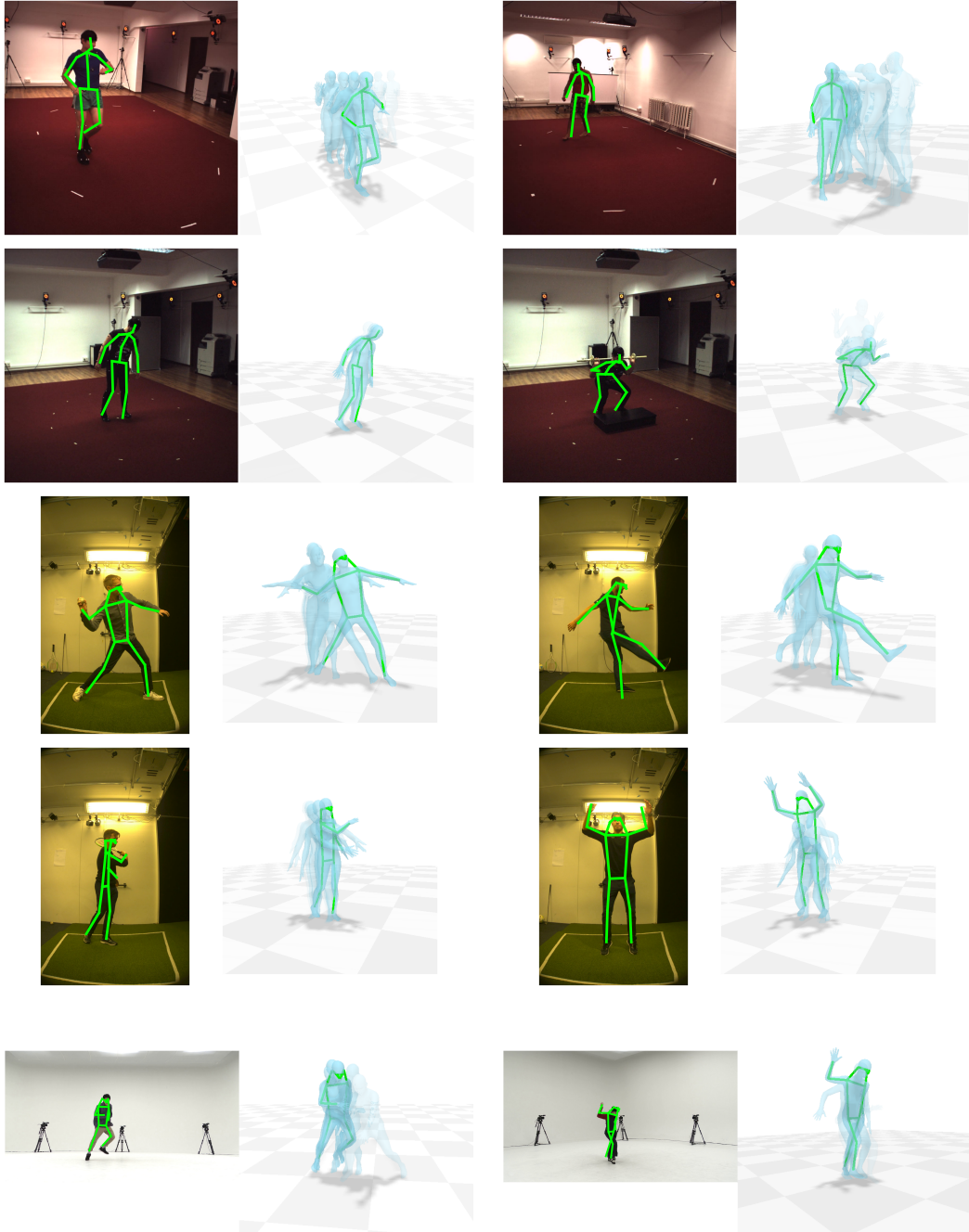


Figure 7: Additional qualitative results on Human3.6M (first row), Fit3D (second row), SportsPose (third and fourth rows), and AIST (last row). The transparency of 3D poses corresponds to their time stamps in the motion sequence. The 2D projections (2D green) is obtained by multiplying camera intrinsic matrix with 3D keypoints (3D green). The Human3.6M 17 keypoints configuration is used for Human3.6M and Fit3D, while the COCO 17 keypoints used for SportsPose and AIST.

C TRAINING DETAILS ON AIST

Unlike the optimization-based approach DiffPhy, our QuaMo is learning-based; therefore, we train QuaMo on 10 random samples from the provided training data of AIST, which are different from the 15 test sequences suggested by Gartner et al. (2022a). To keep a fair comparison, we also train and test on only the first 120 frames of the respective sequences. The details about the selected training sequences can be found in Tab. 5.

Sequence	Frames
gHO_sFM_c01_d19_mHO3_ch04	1-120
gKR_sFM_c01_d28_mKR3_ch04	1-120
gLH_sFM_c01_d16_mLH3_ch04	1-120
gMH_sBM_c02_d24_mMH3_ch03	1-120
gMH_sBM_c03_d24_mMH3_ch06	1-120
gMH_sBM_c04_d24_mMH3_ch01	1-120
gMH_sBM_c05_d24_mMH3_ch07	1-120
gMH_sBM_c06_d24_mMH3_ch05	1-120
gMH_sBM_c08_d24_mMH3_ch04	1-120
gMH_sBM_c09_d24_mMH3_ch09	1-120
gMH_sFM_c07_d24_mMH3_ch18	1-120

Table 5: Dancing samples from the AIST dataset are used for training.

D COMPUTATIONAL COMPLEXITY

QuaMo is designed to be a real-time approach that takes in single-frame input and outputs next frame estimation. The number of parameters of InitNet is 62361, and ControlNet is 559074. In total, QuaMo has 621435 learnable parameters, which is significantly lower than 7.2M parameters of the competitive approach OSDCap. The per-frame processing time of QuaMo is **5.74**ms on the NVIDIA A100, 7.15ms on the NVIDIA Tesla T4, significantly faster than \approx 25ms of OSDCap.

E APPROXIMATION OF QUATERNION INTEGRATION

Prior work, *i.e.* NeurPhys or OSDCap, approximate the next quaternion solution q_{t+1} given the current quaternion q_t and the current angular velocity ω_t via the following equations

$$\begin{aligned} \dot{q}_t &= q_t \otimes \left(0, \frac{1}{2} \omega_t \right), \\ q_{t+\Delta t} &= q_t + \dot{q}_t \Delta t, \\ q_{t+\Delta t} &= q_{t+\Delta t} / \|q_{t+\Delta t}\|. \end{aligned} \tag{7}$$

The integration scheme in Eq. 7 essentially moves the quaternion outside the sphere \mathcal{S}^3 and thus requires the magnitude renormalization. This introduces high error during integration, especially for long human motion sequences. The correct method for computing the next quaternion solution is addressed in Sec.3.2 of the main paper, and it effectively reduces the error of captured motions.

F GLOBAL TRANSLATION ANALYSIS

We plot two examples of root translation in world coordinate in Fig. 8. The root translation is computed via Euler’s integration, described in Sec.3.3 with $\Delta t = 0.04$, the real-time transitioning of a motion capture sequence of 25Hz. Previous work, such as NeurPhys Shimada et al. (2021), splits the integration into six iterations, causing the numerical errors from Euler’s method to build up and accumulate over each iteration, while QuaMo does not have this problem. Fig. 8 clearly demonstrates the performance gains that QuaMo provides, in both accuracy and smoothness with respect to the ground truth trajectory.

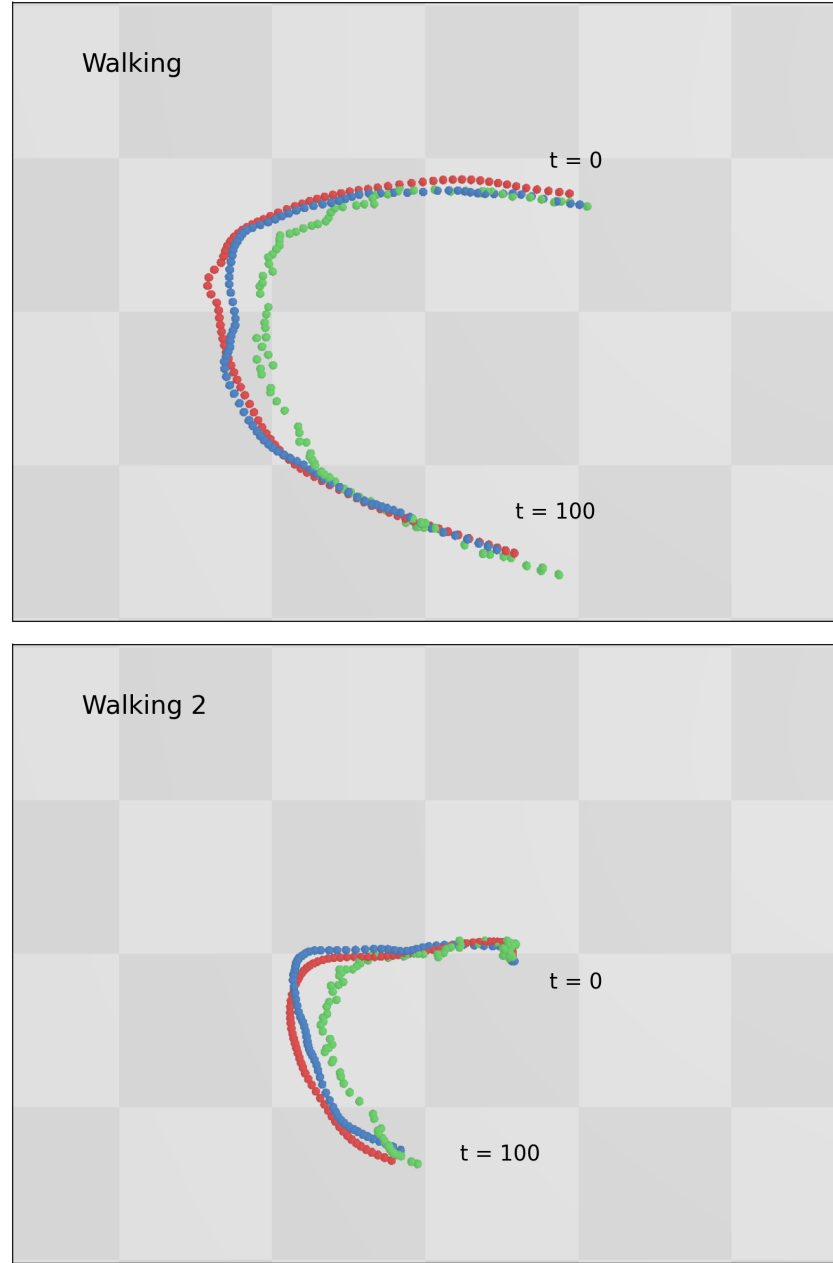


Figure 8: Root trajectory comparison between QuaMo (blue), input signals from TRACE (green), and ground truth (red). QuaMo provides a highly smooth and accurate root trajectory estimation, with no numerical error.